nature communications

Article

https://doi.org/10.1038/s41467-025-59808-w

High performance relaxor ferroelectric textured ceramics for electrocaloric refrigeration

Received: 16 January 2025

Accepted: 6 May 2025

Published online: 17 May 2025

Check for updates

Xuexin Li[1], Jinglei Li[1,2] ✉, Yang Li[1], Xuechen Liu[1], Shuai Yang[1], Jie Wu[1], Dingwei Hou[1], Jinjing Zhang[1], Haijun Wu[3], Yang Zhang[1,4], Xiangdong Ding[3], Jun Sun[3], Shujun Zhang[5], Hongliang Du[6] ✉ & Fei Li[1,2] ✉

Relaxor ferroelectric ceramics have emerged as promising candidates for electrocaloric cooling systems due to their relatively higher heating and cooling capacities. However, simultaneously achieving high temperature changes (ΔT) and a wide operating temperature range remains a significant challenge, limiting their practical applications. This work proposes a synergistic strategy that involves precise compositional tuning of the $BaTiO_3$-$x KNbO_3$ system to customize the rhombohedral-to-cubic phase boundary around room temperature, coupled with engineering grain orientation of the ceramics. Based on this approach, a maximum ΔT of 3.9 K is achieved in $<111>_c$-texture $BaTiO_3$-$KNbO_3$ ceramics, outperforming most environmentally friendly ceramics. Notably, the ΔT variation remains within ±10% across a temperature range of 30 °C to 80 °C, demonstrating a promising material for the design and application of electrocaloric cooling devices. This work provides new insights for the design of ceramics with optimized electrocaloric properties, offering significant potential for improving the efficiency and functionality of next-generation cooling technologies and devices.

Electrocaloric effect (ECE) has been drawing remarkable and intense attention as one promising alternative to the conventional cooling technology based on a vapor compression cycle in order to decrease CO_2 emissions[1–3]. Polar materials are core components of electrocaloric refrigerant devices and directly determine their performance[4,5]. Among various polar materials used for electrocaloric cooling, due to their high electrocaloric effect and wide operating temperature range, relaxor ferroelectric ceramics are considered as one of the most promising candidates[6–9]. Consequently, research on high-performance relaxor ferroelectric ceramics has become a key focus, emphasizing on domain engineering, compositional optimization, and defects design to enhance electrocaloric properties for practical applications.

The Gibbs free energy of a ferroelectric material can be written as an expansion utilizing polarization as the order parameter[10–12]:

$$G = \frac{1}{2}\alpha P^2 + \frac{1}{4}\xi P^4 + \frac{1}{6}\zeta P^6 - EP \quad (1)$$

where P is the polarization, $\alpha = \beta(T - T_0)$, ξ and ζ is a constant independent of temperature. The isothermal entropy change (ΔS) and adiabatic temperature variation (ΔT_{ECE}) under electric field were

[1]Electronic Materials Research Laboratory (Key Lab of Education Ministry), State Key Laboratory for Mechanical Behavior of Materials and School of Electronic and Information Engineering, Xi'an Jiaotong University, Xi'an, China. [2]State Industry-Education Integration Center for Medical Innovations, Xi'an Jiaotong University, Xi'an, China. [3]State Key Laboratory for Mechanical Behavior of Materials, Xi'an Jiaotong University, Xi'an 710049, China. [4]Instrumental Analysis Center of Xi'an Jiaotong University, Xi'an Jiaotong University, Xi'an 710049, China. [5]Institute of Superconducting and Electronic Materials, Australian Institute for Innovative Materials, University of Wollongong, Wollongong, NSW 2500, Australia. [6]Multifunctional Electronic Ceramics Laboratory, College of Engineering, Xi'an International University, Xi'an 710077, China. ✉e-mail: lijinglei@xjtu.edu.cn; duhongliang@126.com; ful5@xjtu.edu.cn

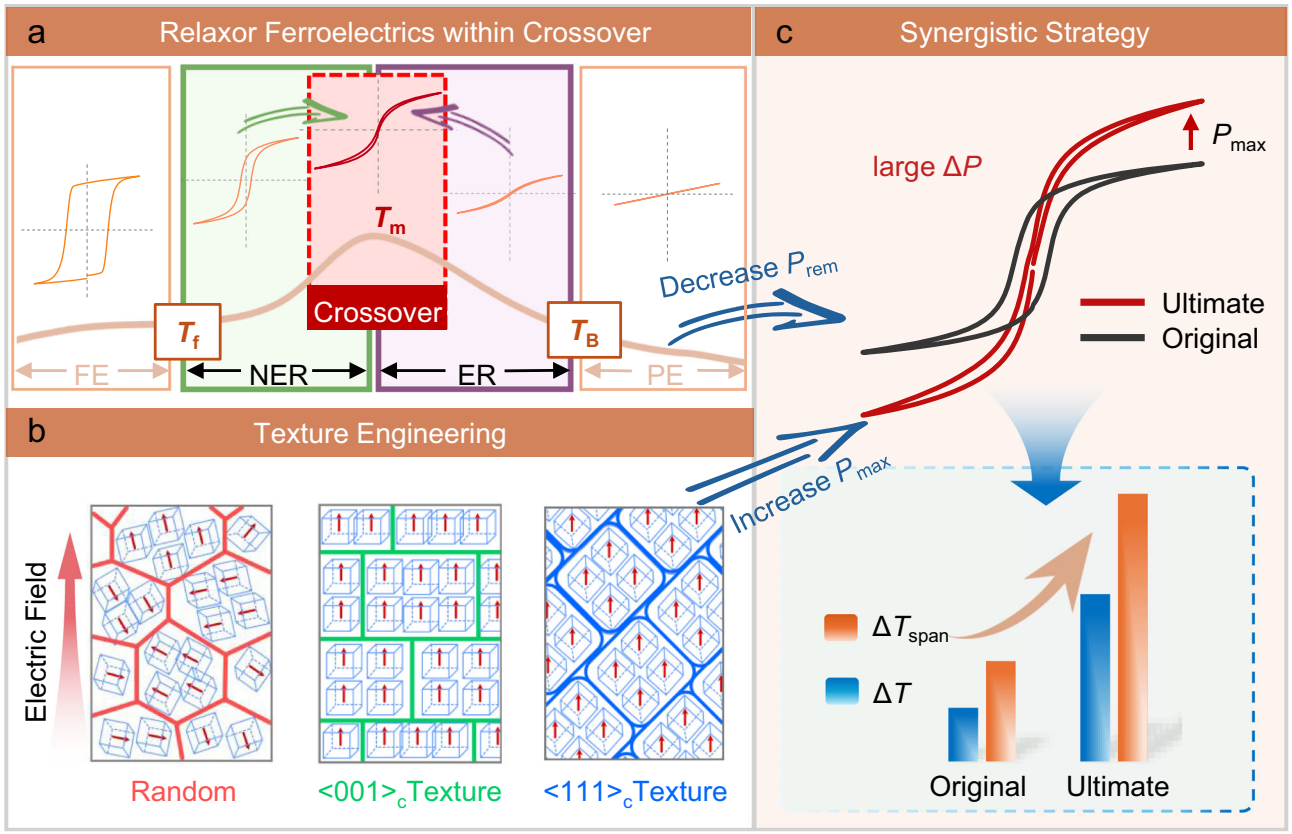

Fig. 1 | Schematic diagram of enhancing ECE properties through−achieving the crossover polar state and texturing the grains of BT-KN ceramics. a Schematic diagram of temperature-dependent ferroelectric and dielectric properties of relaxor ferroelectric materials. **b** Schematic representation of grain orientation of ceramics. **c** An illustration of the expected *P*–*E* behavior and electrocaloric effect based on the proposed synergistic strategy.

derived from the fundamental thermodynamic relationship $\Delta S = -\left(\frac{\partial G}{\partial T}\right)_{E,X}$, as explicitly formulated in Eqs. (2) and (3):

$$\Delta S = -\frac{1}{2}\beta(P_{max} - P_{rem})^2 \quad (2)$$

$$\Delta T_{ECE} = \frac{T}{c_E}\Delta S = \frac{T}{2c_E}\beta(P_{max} - P_{rem})^2 \quad (3)$$

where T denotes the temperature, ΔS represents the entropy change, and c_E is the specific heat capacity. β refers to a Landau free energy coefficient. For a ferroelectric material at paraelectric phase, the dielectric stiffness is a product of $(T-T_0)$ and β. P_{max} and P_{rem} are the maximum and remnant polarizations observed during the application and removal of an electric field, respectively. Essentially, ECE originates from the change in the degree of ordering of the polar state under the action of an electric field, i.e., the entropy change (ΔS)[13–15]. For ferroelectrics, the ΔS under the application of an electric field can be characterized by the product of the phenomenological coefficient β and the polarization change $\Delta P = P_{max} - P_{rem}$[16,17]. Therefore, achieving a high ECE presents a significant challenge in the design of ceramics with both high β and large ΔP across a wide temperature range.

To achieve high β, we selected $BaTiO_3$-$KNbO_3$ (BT-KN) solid-solution as a basic material system due to the following reasons. First, both $BaTiO_3$ and $KNbO_3$ end-members possess a high phenomenological coefficient β, being 4.12×10^5 C^{-2} m^2 N and 4.273×10^5 C^{-2} m^2 N, respectively, which are the highest values among reported lead-free ferroelectrics[18,19]. Second, $BaTiO_3$-$KNbO_3$ solid-solutions possess diverse temperature-induced phase transitions and relaxor ferroelectric characteristics, which offer a great possibility for achieving a high ECE in a wide temperature range[20].

As illustrated in Fig. 1a, relaxor ferroelectrics can be divided into four regions based on their dielectric behavior, that are paraelectric (PE), ergodic relaxor state (ER), nonergodic relaxor state (NER), and ferroelectric states (FE)[21–23]. During cooling, highly dynamic polar nanoregions (PNRs) emerge upon crossing the Burns temperature (T_B), with the correlation length of dipoles increasing as the temperature decreases, leading to a significant enhancement in P_{max}. Below the freezing temperature (T_f), the polar state transitions into a mixed ferroelectric-glass state, where the *P*–*E* loop evolves into a characteristic square-shaped hysteresis curve, resulting in both large P_{max} and P_{rem}.

To achieve a large ECE across a wide temperature range, our strategy is to shift the temperature of maximum permittivity (T_m) around room temperature, creating a crossover region between the ergodic and nonergodic relaxor states for BT-KN solid-solution. This configuration offers two critical advantages: (1) a near-linear *P*–*E* loop in the crossover region, enabling the maximization of ΔP; (2) the dynamic evolution of PNRs across a broad temperature range, significantly extending the operational temperature range of electrocaloric ceramics.

Moreover, perovskite ferroelectrics exhibit pronounced anisotropy, and thus controlling grain orientation can significantly optimize their properties. Previous studies have demonstrated the impact of crystal orientation on ECE for perovskite ferroelectrics. For example, Bai et al. investigated the ECE in $0.7Pb(Mg_{1/3}Nb_{2/3})O_3$–$0.3PbTiO_3$ (PMN-30PT) single crystals and found that near the rhombohedral-to-cubic (R–C) phase transition point, the ECE of the $[111]_c$-oriented crystal exceeded that of the $[001]_c$-oriented crystal by 11%[24]. Similarly,

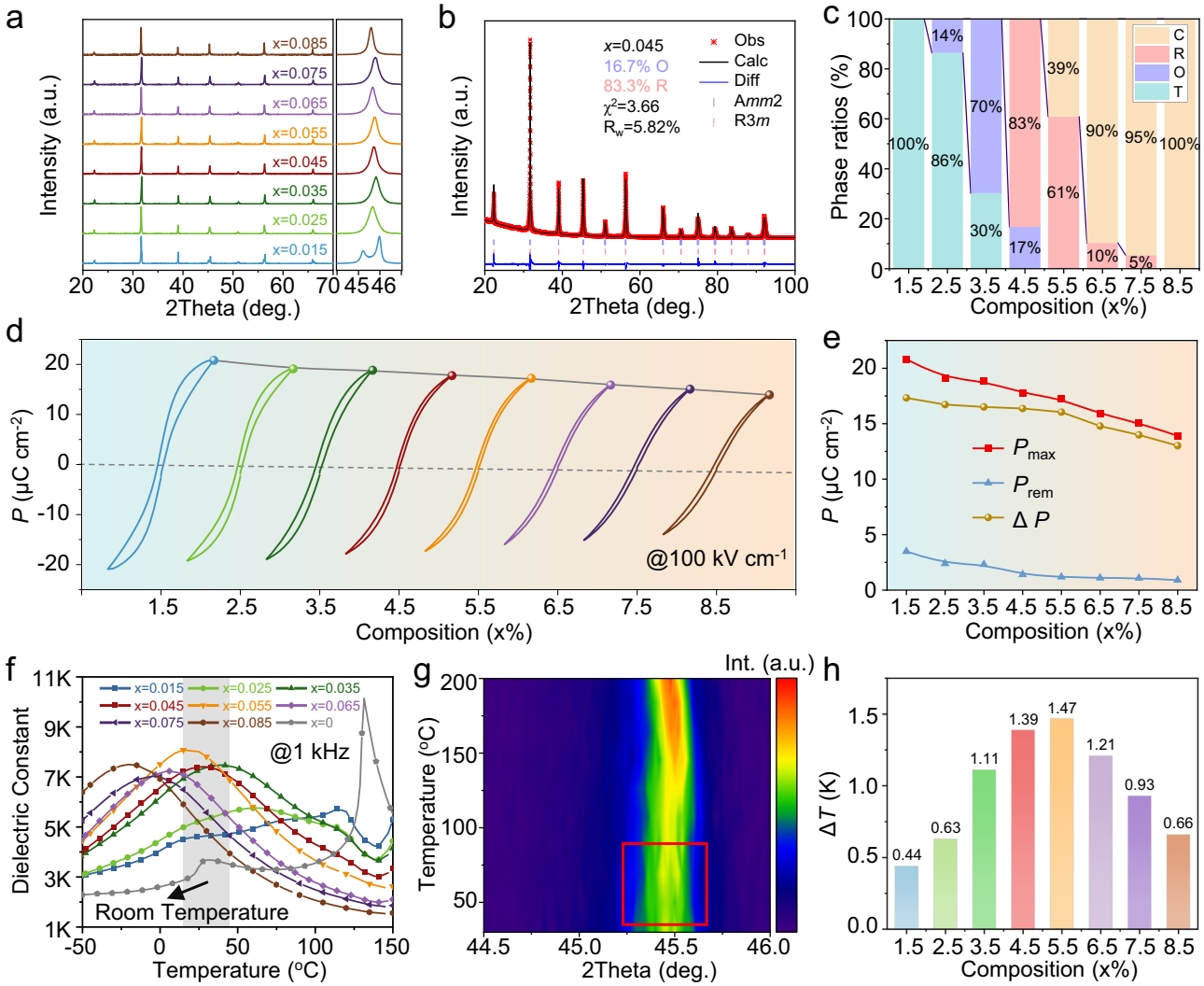

Fig. 2 | Phase structure, polarization-electric-field behaviors, dielectric properties and ECE performances of $(1-x)BaTiO_3$-$xKNbO_3$ ($x = 0.015$–0.085) ceramics. a Room temperature XRD patterns; **b** XRD pattern of $x = 0.045$ as Rietveld refinement; **c** The variation of phase content as a function of composition; **d** Room temperature hysteresis loops; **e** P_{max}, P_{rem}, and ΔP for various compositions; **f** Temperature dependence of dielectric properties; **g** XRD pattern of $x = 0.045$ as a function of temperature; **h** ΔT dependence under the electric field of 100 kV cm^{-1} for various compositions. (Full details of the measurement protocol are documented in Supplementary Note 1).

Chen et al. studied the ECE of $Pb(Zn_{1/3}Nb_{2/3})O_3$-$PbTiO_3$ (PZN-PT) single crystals and observed that the ECE of $[111]_c$-oriented crystals were 38% higher than that of $[011]_c$-oriented crystals[25]. These findings suggest that fabrication of ceramics with aligned grain orientation (i.e., textured ceramics, as shown in Fig. 1b) is a possible approach to further enhance the ECE of BT-KN ceramics.

As discussed above, the main idea of our present work is presented in Fig. 1 and introduced as follows. First, by constructing the BT-KN solid-solution, we try to obtain a relaxor ferroelectric system with a high ECE over a wide temperature range. Second, by using template grain growth (TGG) method, we propose to fabricate $<001>_c$ and $<111>_c$ textured BT-KN ceramics for further optimizing their ECE effect.

Results and discussion

Figure 2a illustrates the room-temperature XRD results for the BT-xKN ceramics, with corresponding Rietveld refinements presented in Fig. 2b, Supplementary Fig. S2 and Table S2. All ceramics exhibit the characteristic diffraction peaks of a pure perovskite structure, with no secondary phases detected. For $x = 0.015$, the splitting of the (200) peak in the XRD data indicates a tetragonal phase. For $x > 0.015$, the splitting of the (200) peak in the ceramics is not easy to be distinguished. However, the unsymmetrical characteristic of the (200) peak is detectable, which indicates the potential coexistence of multiple phases[26,27]. The phase structure of the BT-xKN ceramics at room temperature is shown in Fig. 2c. Due to the similarity in phase transition sequences and crystal structures between $KNbO_3$ and $BaTiO_3$ (with the central Nb^{5+} or Ti^{4+} being disordered), the phase structure and relaxor behavior of $BaTiO_3$ are highly sensitive to the content of $KNbO_3$. The introduction of low concentrations ($x \le 0.045$) of $KNbO_3$ leads to a gradual transformation of the tetragonal phase in BT-xKN ceramics into orthorhombic and rhombohedral phases. Further increasing the $KNbO_3$ content promotes a transition towards cubic phase. The symmetry of the rhombohedral structure is much lower than that of the cubic structure, which makes the rhombohedral-to-cubic (R–C) phase transition involve substantial structural rearrangements, resulting in a large change in free energy. This process contributes to enhanced the ECE in the ceramics[28,29].

To investigate the ferroelectric properties of (1-x)BT-xKN ceramics at different stages, bipolar hysteresis loops were measured at room temperature under an electric field of 100 kV cm^{-1}, as shown in Fig. 2d. At $x = 0.015$, the ceramic is in the FE state, larger P_{rem} and P_{max} can be obtained in the hysteresis loop, accompanied by larger

hysteresis. At $x = 0.025$ and 0.035, the ceramics transition into the NER state, the P_{rem} decreases, and the hysteresis loop reveals characteristic features of a relaxor ferroelectric. For $x = 0.045$ and 0.055, the ceramics exists in a crossover region between the NER and ER states, maintaining a stable ΔP over a wide temperature range with low hysteresis. The variations of P_{max}, P_{rem}, and ΔP with $KNbO_3$ concentrations are shown in Fig. 2e. At $x \geq 0.065$, the ceramics gradually transitions from the ER to PE state, with the hysteresis loop showing lower P_{max} and a nearly linear hysteresis loop.

Figure 2f presents the temperature-dependent dielectric properties of the (1-x)BT-xKN system at varying $KNbO_3$ doping levels. At $x = 0.015$, three dielectric anomalies are observed, corresponding to rhombohedral-to-orthorhombic (R–O), orthorhombic-to-tetragonal (O–T), and tetragonal-to-cubic (T–C) phase transitions. Similar to the XRD results, as the $KNbO_3$ content increases, the tetragonal-to-cubic transition is suppressed, and T_m shifts to lower temperatures. At $x = 0.045$, the peak associated with the T–C phase transition completely disappears, and a single broad dielectric peak is observed throughout the entire temperature range[30]. The dielectric relaxation coefficient (γ) at 1 MHz is 1.90 (Supplementary Fig. S4), indicating typical relaxor ferroelectric behavior. This observation is consistent with the changes observed in the XRD (200) diffraction peak shown in Fig. 2g, where a diffused phase transition is observed between 20–80 °C. This result also confirms the formation of a crossover region between the NER and ER states near room temperature for $x = 0.045$, thereby broadening the operational temperature range of the ECE[31].

Figure 2h shows the electrocaloric performance of (1-x)BT-xKN ceramics at room temperature. The maximum electrocaloric performance occurs at $x = 0.055$, but its low T_m limited the operating temperature range ΔT_{span}. In contrast, the $x = 0.045$ composition demonstrates $T_m \approx 32$ °C and a peak ΔT spanning 30–50 °C, aligning with solid-state cooling applications (e.g., electronics thermal management, residential cooling). Considering operational stability and the broader working temperature range (ΔT_{span}) compared to the $x = 0.055$ variant, the $x = 0.045$ composition was selected for further optimization to ensure enhanced temperature-stable electrocaloric properties.

To further enhance the ECE of $BaTiO_3$-0.045$KNbO_3$ ceramics, crystal anisotropy was utilized in this work. We employed the templated grain growth (TGG) method to fabricate $BaTiO_3$-0.045$KNbO_3$ (referred to as BT-45KN) ceramics with $<001>_c$ and $<111>_c$ orientations. However, the substitution of Ti^{4+} sites (ionic radius: 0.605 Å) by Nb^{5+} ions (ionic radius: 0.64 Å) induced significant lattice distortion during sintering. The mismatch of ionic radii inhibited the grain growth (Supplementary Fig. S5). Moreover, traditional titanate templates often react with $BaTiO_3$ and $KNbO_3$ in the solid phase and the volatility of potassium leads to the formation of a secondary phase (Supplementary Fig. S6). The mismatch of ionic radii inhibited the coarsening of the crystals. Therefore, balancing the reaction rate of grain growth induced by the template with the enhancement of template stability is crucial. Generally, the smaller the matrix grain, the faster the textural growth process[32,33]. To facilitate texturing process, we reduced the matrix powder size to approximately 90 nm (Supplementary Fig. S7) and added 0.5 wt% MnO_2 during the tape-casting process to inhibit the valency change of titanium[34,35].

We synthesized high aspect ratio $(001)_c$ and $(111)_c$ $BaTiO_3$ templates based on an improved topotactic chemistry approach[36,37]. By uniformly distributing plate-like templates on quartz, XRD spectra of $(001)_c$ and $(111)_c$ $BaTiO_3$ templates were obtained. The templates displayed characteristic double peaks near 45°, indicative of a typical tetragonal structure, with no secondary phases detected in any of the products. Statistical analysis of length and thickness data for all products was performed using particle size distribution software, as shown in Supplementary Fig. S8. The synthesized $BaTiO_3$ templates not only possess the high aspect ratios of precursors from topological transformation reactions but also maintained high purity (Supplementary Fig. S9). With length-to-thickness ratios exceeding 12, the $BaTiO_3$ templates are highly suitable as templates for textured ceramics.

To assess the influence of templates on ferroelectric properties, we synthesized non-oriented BT-45KN ceramics using an equivalent number of templates for comparison. Figure 3a–c display the X-ray diffraction patterns of random, $<001>_c$ textured and $<111>_c$ textured BT-45KN ceramics. All samples exhibited pure perovskite phases. The Lotgering factors $F_{001} = 94\%$ and $F_{111} = 84\%$, demonstrating a pronounced preferential orientation of the grains. Electron backscatter diffraction (EBSD) images in Fig. 3d–f further verified the substantial increase in the number of oriented grains in textured samples compared to their non-textured counterparts. During the texturing process, fine grains of the matrix dissolved and precipitated on the template surfaces, driven by the differential surface energies between the templates and matrix grains, which also resulted in varied growth rates along specific directions[38,39]. SEM images in Fig. 2d–f illustrate the cross-sections of both random and textured samples, showing that the $(001)_c$ and $(111)_c$ $BaTiO_3$ templates effectively guided the nucleation and epitaxial growth of oriented BT-KN grains on their surfaces, resulting in the formation of differently shaped textured grains along the respective texturing directions. Notably, the $<111>_c$ oriented grains were significantly larger than those of the $<001>_c$ orientation, a consequence of the size differences between the $(001)_c$ and $(111)_c$ $BaTiO_3$ templates (Supplementary Fig. S10).

Understanding the relationship between the ECE and phase transitions represents a pivotal advancement in enhancing the efficiency of solid-state cooling devices. Figure 4a depicts the temperature dependence of dielectric properties for BT-45KN ceramics with random grains, $<001>_c$, and $<111>_c$ textured grains. The maximum dielectric constant (ε_m) for all samples shows a peak around 44 °C, facilitated by the homogeneous texture process ensuring compositional uniformity. Figure 4b shows the polarization-electric field (P–E) loops under the electric field of 100 kV cm^{-1} at various temperatures. In the temperature range suitable for EC refrigeration applications (20–80 °C), the $<111>_c$ textured BT-KN ceramics exhibit slim P–E loops, which results in lower P_{rem} and loss. Low loss reduces joule heating during the EC devices operation, resulting in higher energy efficiency. Similar to the P–E characteristics, the bipolar S–E curves of ferroelectric crystals also depend on crystal orientation. Under an electric field of 100 kV cm^{-1}, strain in $<001>_c$ textured samples reach a maximum of 0.34%, followed by random ceramics at 0.15%, while strain in $<111>_c$ textured samples is minimal at 0.08%. This phenomenon can be attributed to the fact that lowest electrostrictive coefficient Q_{33} is along the $<111>_c$ direction for ABO_3 perovskite crystals[40]. In $<111>_c$ textured ceramics, the reduced electrostrictive strain effectively minimizes internal deformation and stress-induced microcracks. This structural improvement enhances the breakdown field strength, thereby improving the operational stability and extending the service life of EC devices[41].

Figure 4c illustrates the temperature-dependent relationships of P_{max} and P_{rem} for the ceramics. The polarization decreases with increasing temperature for all samples, with the highest P_{max} and lowest P_{rem} observed in $<111>_c$-textured BT-KN ceramics, favoring larger electrocaloric effect. It is noteworthy that both the hysteresis loops and the strain show a pronounced orientation dependence. This is because, when an electric field (exceed the coercive field) is applied, the dipoles will aligned to the direction close to the applied electric field, particularly along the potential polar axis in ferroelectric ceramics[42,43]. For instance, in the rhombohedral crystal, there are eight possible polarization directions along the diagonal <111> of the unit cell. As shown in Fig. 4d, upon the application of a strong enough electric field along the $[001]_c$ direction, four of these eight domains are

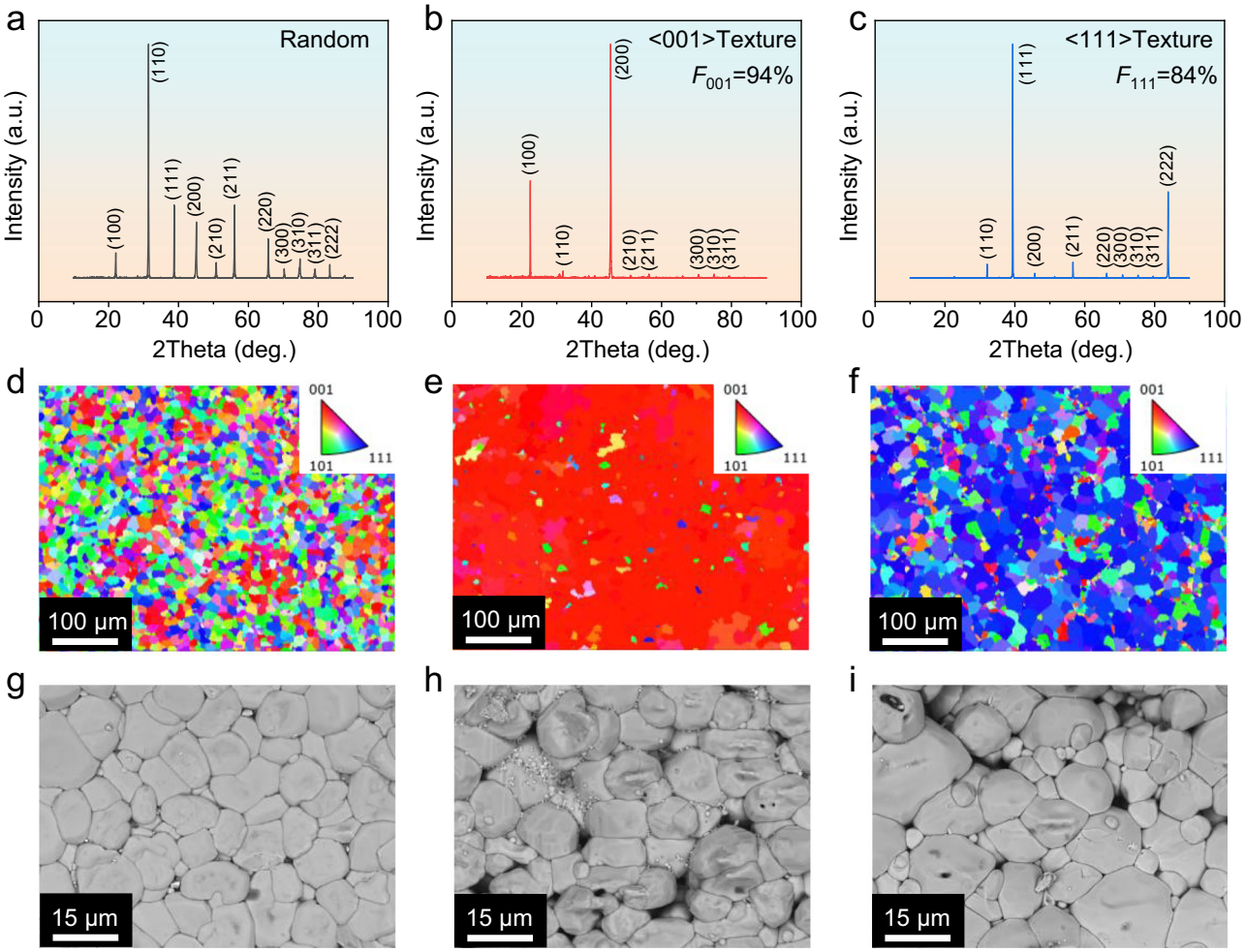

Fig. 3 | Microstructures of textured and non-textured BT-KN ceramics. a–c X-ray diffraction patterns corresponding to different orientations. **d–f** EBSD results of different-oriented BT-KN ceramics (the test surface of textured samples is parallel to the template). **g–i** SEM images of ceramic surfaces.

energetically favored by a bias energy, forming a "4R" engineered domain structure. In contrast, when an electric field is applied along the <111> direction, only a single polar vector exists in this orientation, leading to the formation of a monodomain state, referred to as "1R"[44]. The rhombohedral phases exhibit superior polarization performance when an electric field is applied along the $[111]_c$ direction. For $BaTiO_3$-$KNbO_3$ ferroelectric ceramics with $<111>_c$ texture near room temperature, the rhombohedral and orthorhombic phases dominate. Consequently, the field-induced polarization near room temperature shows the highest value of 18.9 μC cm^{-1} in $<111>_c$ textured samples and the lowest value of 15.9 μC cm^{-1} in $<001>_c$ textured samples (Supplementary Fig. S11).

Figure 5a illustrates the heat flow curves of $<111>_c$ textured BT-45KN ceramics under various electric fields and temperatures. The electrocaloric effect signal is acquired using heat flux sensors in close contact with the material surface, spanning the entire active area of the samples. A pronounced exothermic peak occurs with the application of an electric field during the positive electrocaloric effect, whereas an endothermic peak emerges upon the field's removal, as shown by the respective upward and downward peaks in the figure. For precise measurement of the thermal signal, calibration is performed against reference heat released by electrodes (Supplementary Note 1). Over the course of testing, the heat flux curves across all temperature ranges revert to baseline after a period, indicating the stability of the samples at elevated temperatures without the generation of joule heating[45,46].

Figure 5b and c illustrates the relationship between ΔT and ΔS of BT-45KN ceramics with varying orientations in relation to temperature and electric field. Apart from the orientation of the $BaTiO_3$ template, the composition and preparation processes of samples used for electrocaloric performance testing were consistent. At 50 °C, $<111>_c$ textured BT-45KN ceramics reached a ΔT of 3.9 K and ΔS of 5.5 J kg^{-1} K^{-1}. Beyond their high electrocaloric performance near room temperature, these applications also require excellent temperature stability. Typically, the operational temperature range (T_{span}) for electrocaloric materials is defined as ΔT exceeding 90% of ΔT_{max}, as demonstrated by the region encompassed in the curve in Fig. 5b. Encouragingly, through a synthesis of chemical engineering and crystal orientation strategies, $<111>_c$ textured BT-45KN ceramics not only exhibit a high ΔT near room temperature but also demonstrate a broad operational temperature range of at least 50 K (-30 to 80 °C). Figure 5d shows the trends of ΔT with temperature under an electric field of 200 kV cm^{-1} for different orientations of textured BT-45KN ceramics. The homogenous texturing process minimizes the impact of the fabrication process on ceramic performance. With only crystal orientation altered, the electrocaloric performance of $<111>_c$ textured BT-45KN ceramics significantly improved by 11% compared to non-textured ceramics. Compared to recently reported ECE ceramics (Fig. 5e), the $<111>_c$ textured BT-45KN samples not only exhibit exceptionally high ΔT near room temperature but also maintain a broad application temperature range, indicating a clear advantage in the field of environmentally friendly electrocaloric cooling ceramics.

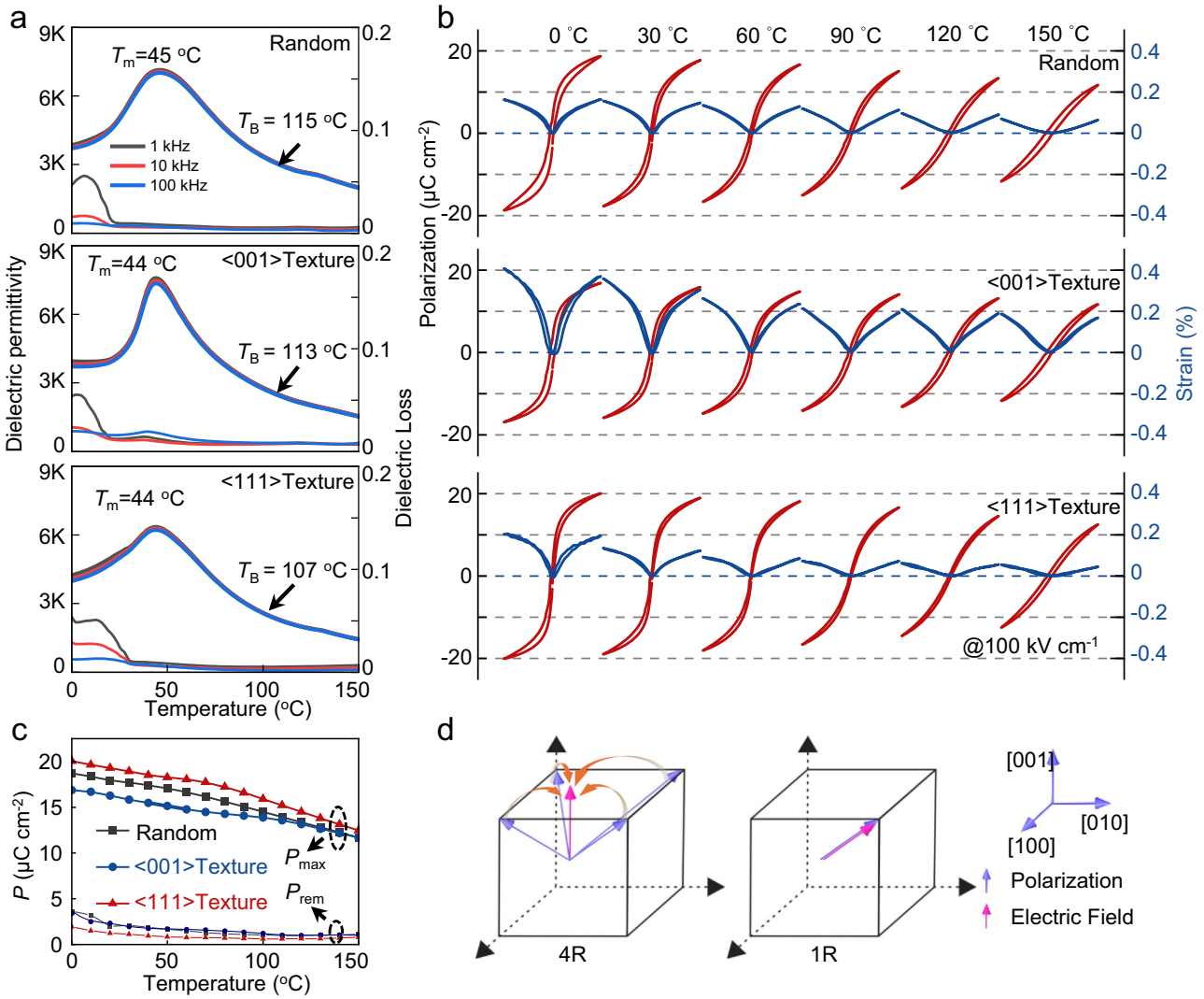

Fig. 4 | Dielectric and ferroelectric properties of textured and non-textured BT-45KN ceramics at different temperatures. a Dielectric temperature spectrum; **b** Hysteresis loops and strain curves; **c** The variation of P_{max} and P_{rem}; **d** Possible domain engineered structures formed in rhombohedral perovskites by poling at high fields along $[001]_c$ and $[111]_c$ directions.

In the present work, in order to tackle the long-standing challenge of synthesizing novel electrocaloric ceramics, we present an analysis based on the Landau-Devonshire phenomenological theory, which introduces a design strategy focused on maximizing the β coefficient and ΔP through enhancing polarization changes induced by the electric field. Based on this idea, we design and fabricate <111>c-textured BT-KN relaxor ferroelectric ceramics, which show temperature variations ΔT higher than 3.3 K over a wide operational temperature range (30 to 80 °C). The remarkable ECE performance makes our newly developed ceramics a promising candidate for emerging solid-state refrigeration applications. Future efforts will focus on translating this breakthrough into functional devices through scalable texturing techniques, optimized thermal interfaces for rapid heat exchange, and enhanced cycling durability, as critical steps toward realizing efficient, reliable, and eco-friendly electrocaloric cooling systems.

Methods

Synthesis of BT-KN ceramics

The (1-*x*)BT-*x*KN ceramics were prepared using the conventional solid-state sintering method. The starting materials, including $BaTiO_3$ (particle size <100 nm, 99.9%, Aladdin), K_2CO_3 (99.9%, Aladdin), and Nb_2O_5 (99.99%, Aladdin), were processed through wet milling (zirconia media, ethanol solvent) in nylon containers at 300 rpm for 12 h. After drying, the homogeneous mixture was calcined at 950 °C in air for 3 h.

The calcined powders were subsequently processed through planetary ball milling at 450 rpm for 6 h, followed by drying and sieving through 120-mesh sieve. This mechanical treatment effectively utilized shear and collision forces to break agglomerates and refine the particles to a target size of ~90 nm. The resultant powders were uniaxially pressed into disk-shaped compacts (8 mm diameter × 1 mm thickness) under 1 MPa pressure. These green samples were vacuum-sealed and subjected to cold isostatic pressing at 220 MPa for 10 min to enhance their mechanical strength. The samples were subsequently sintered in air at temperatures ranging from 1240 °C to 1300 °C for 2 h to yield (1-*x*)BT-*x*KN bulk ceramics. To implement the potassium volatilization suppression strategy, the sintering process incorporated two containment measures: (1) Complete encapsulation of green samples within pre-calcined powder bed, creating chemical potential equilibrium to minimize elemental loss. (2) Hermetic sealing using alumina crucibles (20 mm diameter × 20 mm height) as primary containment vessels.

Synthesis of $(001)_c$ and $(111)_c$ $BaTiO_3$ templates

The $(001)_c$ and $(111)_c$ $BaTiO_3$ templates were synthesized using a two-step topochemical reaction method. The reaction equation for the

https://doi.org/10.1038/s41467-025-59808-w

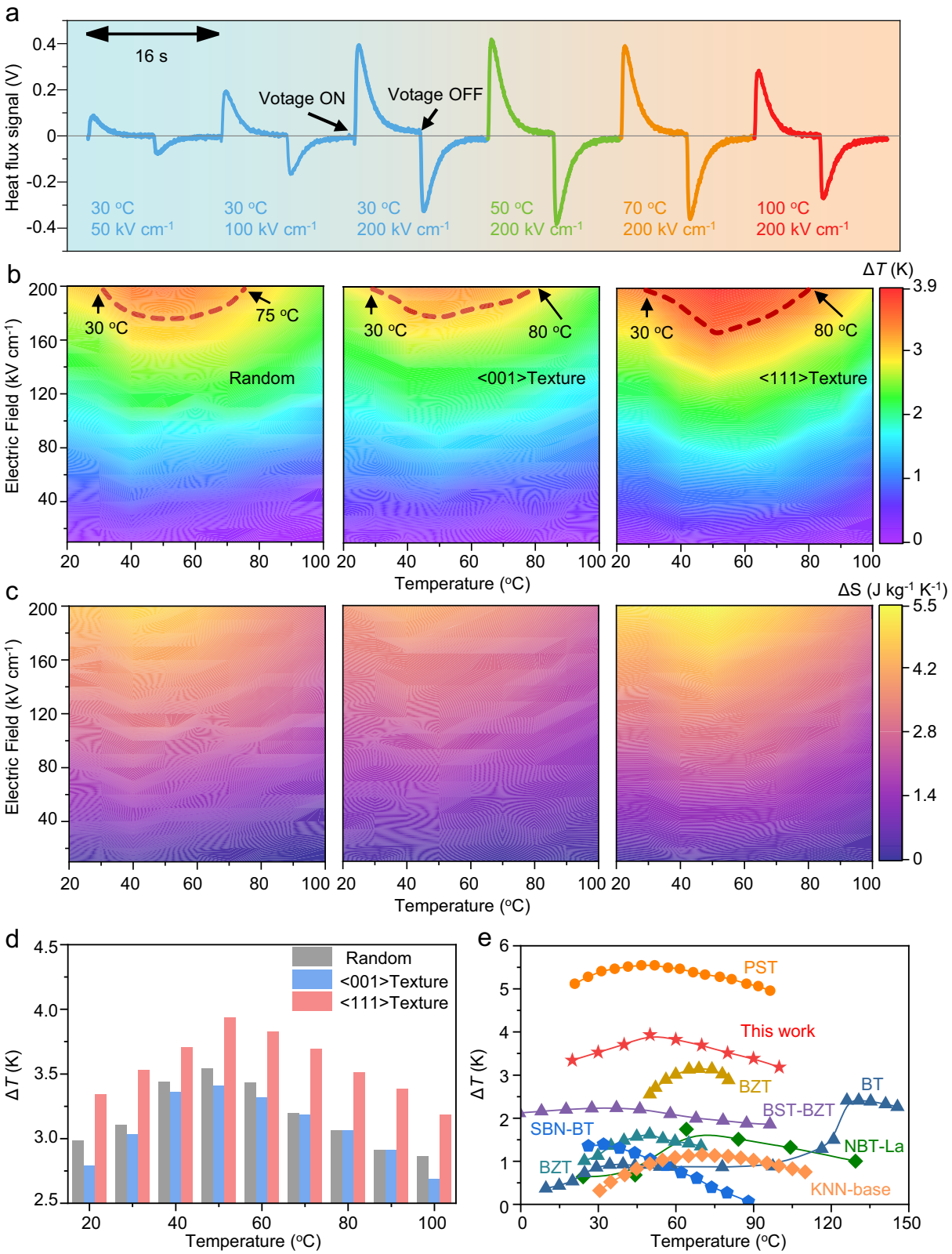

Fig. 5 | Temperature stability of the large ECE. a EC signals (the signal is acquired through a heat flux sensor during voltage shutdown) for <111>$_c$ textured ceramics under different test conditions; **b** ΔT and **c** ΔS for random, <001>$_c$ and <111>$_c$ textured ceramics; **d** At 200 kV $_c$m^{-1}, the EC performance of oriented BT-45KN textured ceramics varies with temperature. **e** Comparison of ECE within electrocaloric ceramics[4,48–54].

synthesis of $(001)_c$ $BaTiO_3$ is as follows:

$$2Bi_2O_3 + 3TiO_2 = Bi_4Ti_3O_{12} \quad (4)$$

$$Bi_4Ti_3O_{12} + 3BaCO_3 = 3BaTiO_3 + 2Bi_2O_3 + 3CO_2 \quad (5)$$

Initially, high-purity Bi_2O_3 (99.99%, Aladdin) and TiO_2 (99.99%, Aladdin) were homogeneously mixed in a molar ratio of 2:3, and an equal mass of salt (NaCl:KCl in a 1:1 mass ratio) was added. The mixture was reacted in a sealed alumina crucible at 1100 °C for 6 h. The product was washed with hot deionized water to remove NaCl and KCl, followed by filtration and drying to obtain $Bi_4Ti_3O_{12}$ templates. In subsequent steps, $Bi_4Ti_3O_{12}$ was combined with $BaCO_3$ (99.8%, Aladdin) at a 1:10 molar ratio, followed by addition of an equal mass of salt (NaCl:KCl in a 1:1 mass ratio). The mixture was thoroughly homogenized and sintered at 1040 °C for 5 h. The resulting product was washed with hot deionized water to remove residual molten salt, then treated with nitric acid to eliminate unreacted Bi_2O_3 and $BaCO_3$, ultimately obtain $(001)_c$ $BaTiO_3$ platelet templates.

The reaction equation for the synthesis of $(111)_c$ $BaTiO_3$ is as follows:

$$6BaTiO_3 + 11TiO_2 = Ba_6Ti_{17}O_{40} \quad (6)$$

$$Ba_6Ti_{17}O_{40} + 11BaCO_3 = 17BaTiO_3 + 11CO_2 \quad (7)$$

Synthesizing $(111)_c$ $BaTiO_3$ began with the homogeneous mixing of $BaTiO_3$ (99.99%, Aladdin) and TiO_2 (99.99%, Aladdin) in a molar ratio of 6:9 (with excess Ba^{2+} added to prevent the formation of secondary phase $Ba_4Ti_{13}O_{30}$), followed by the addition of twice the mass of a salt mixture (NaCl:KCl in a 1:2 mass ratio). The mixture was reacted in a sealed alumina crucible at 1150 °C for 6 h. The product was washed with hot deionized water to remove NaCl and KCl, filtered, and dried to obtain $Ba_6Ti_{17}O_{40}$ templates. Subsequently, $Ba_6Ti_{17}O_{40}$ was mixed with $BaCO_3$ (99.8%, Aladdin) and NaCl in stoichiometric proportions (molar ratio of $Ba_6Ti_{17}O_{40}$ to $BaCO_3$ = 1:12; mass ratio of mixture to NaCl = 1:2). The mixture was reacted at 1150 °C for 4 h, followed by hot deionized water washing to remove NaCl, resulting in $(111)_c$ $BaTiO_3$ templates.

Fabrication of random, $<001>_c$ and $<111>_c$ BT-KN textured ceramics

Non-oriented BT-KN ceramics were synthesized using $(001)_c$ $BaTiO_3$ templates. $0.95BaTiO_3$-$0.05KNbO_3$ matrix powder was chosen for the tape casting process, with the $BaTiO_3$ templates mixed at a 10:1 weight ratio and augmented by 0.5 wt.% MnO_2. After homogeneous mixing, the calcined powder was compacted into disks of 8 mm diameter and 1 mm thickness under a uniaxial pressure of 1 MPa. These green sample were vacuum-sealed and subjected to cold isostatic pressing at 220 MPa for 10 min to enhance their mechanical strength. Finally, the green bodies were sintered at 1250–1300 °C for 2 h, resulting in non-oriented BT-KN bulk ceramics.

BT-KN textured ceramics were fabricated using $(001)_c$ and $(111)_c$ $BaTiO_3$ templates. First, optimal texture and density were achieved by mixing the $BaTiO_3$ templates in a 10:1 weight ratio, selecting $0.95BaTiO_3$-$0.05KNbO_3$ as the matrix powder and adding 0.5 wt.% MnO_2 to inhibit secondary phase formation. Second, the mixed powder was dispersed with ethanol/toluene and KD-1 dispersant at 200 rpm for 24 h to ensure uniform distribution. Polyvinyl butyral (PVB), benzyl butyl phthalate (BBP) and polyethylene glycol (PEG) were then incorporated, and the mixture was further milled for 24 h to prepare the casting slurry. The well-dispersed $(001)_c$ and $(111)_c$ $BaTiO_3$ templates were subsequently added, and the mixture was milled at low speed for 0.5 h. Tape casting was performed using stainless-steel blade set at 180 μm thickness, casting at a rate of 1 cm s^{-1}. Third, the green tapes were cut, precisely aligned, and stacked. To prevent delamination and expansion, the green samples underwent hot isostatic pressing in warm water (75 °C, 30 MPa, 25 min). Fourth, the green sample were then sintered at 600 °C for 4 h to remove organics, followed by a treatment in a mixed argon and oxygen atmosphere in a hot isostatic press furnace at 950 °C for 1 h. Final sintering at 1250–1300 °C for 2 h yielded BT-KN ceramics with $<001>_c$ and $<111>_c$ orientations.

Characterization of structure, morphology, and texture features

Material's microstructure was analyzed using X-ray diffraction (Smartlab, Rigaku, Japan) to determine the crystallographic features. Rietveld refinement via GSAS-II software was employed for precise crystal structure determination. Texture analysis was performed using the Lotgering method[47]. Microstructural characterization including grain orientation and composition distribution was conducted using field-emission scanning electron microscopy (FE-SEM) (GeminiSEM 500), energy-dispersive X-ray spectroscopy (EDS) (UltimMax100, Oxford EDS system, UK), and electron backscatter diffraction (EBSD) (Oxford EBSD System, UK).

Dielectric and ferroelectric performance characterizations

Prior to electrical property testing, both sides of the bulk ceramics were polished, and gold electrodes (12.56 mm^2) were deposited on the ceramic surfaces using magnetron sputtering. The dependence of dielectric constant, dielectric loss, and temperature was measured using an LCR meter (E4980AL, Keysight) being connected to a computer-controlled furnace. Hysteresis loops (P–E) curves, field-induced current density curves (J–E) and field-induced strain curves (S–E) curves were obtained using a ferroelectric analyzer (TF Analyzer 3000, aixACCT, Aachen, Germany). All measurements were conducted under triangular waveform excitation at a test frequency of 1 Hz.

Electrocaloric performance testing

The specific heat capacity (Supplementary Fig. S12) was measured using physical property measurement system(DynaCool, Quantum Design, USA). Electrocaloric measurements were conducted using an electrocaloric testing system (PolyK Technologies, Pennsylvania, USA) with a heat flux sensor (27134–1, RdF Corporation, USA). High voltage was supplied by a Trek 610 C high voltage amplifier. Detailed measurement information can be found in the Supplementary Note 1.

Data availability

All data supporting this study and its findings are available within the article and its Supplementary Information. The data corresponding to this study are available from the first author and corresponding authors upon request.

References

1. Moya, X., Kar-Narayan, S. & Mathur, N. D. Caloric materials near ferroic phase transitions. *Nat. Mater.* **13**, 439450 (2014).
2. Hou, H., Qian, S. & Takeuchi, I. Materials, physics and systems for multicaloric cooling. *Nat. Rev. Mater.* **7**, 633–652 (2022).
3. Qian, X. et al. High-entropy polymer produces a giant electrocaloric effect at low fields. *Nature* **600**, 664–669 (2021).
4. Nair, B. et al. Large electrocaloric effects in oxide multilayer capacitors over a wide temperature range. *Nature* **575**, 468–472 (2019).
5. Liu, C. et al. Phonon entropy engineering for caloric cooling. *Appl. Phys. Rev.* **10**, 031411 (2023).
6. Najmi, F., Yi, W. & Cheng, Z.-Y. Electrocaloric heat pumps using two independently-controlled layers to achieve high cooling power. *Nano Energy* **104**, 107984 (2022).
7. Lheritier, P. et al. Large harvested energy with non-linear pyroelectric modules. *Nature* **609**, 718–721 (2022).

8. Wang, Z. et al. Self-sustaining personal all-day thermoregulatory clothing using only sunlight. *Science* **382**, 1291–1296 (2023).
9. Valant, Matjaz Electrocaloric materials for future solid-state refrigeration technologies. *Prog. Mater. Sci.* **57**, 980–1009 (2012).
10. Shi, J. et al. Electrocaloric cooling materials and devices for zero-global-warming-potential, high-efficiency refrigeration. *Joule* **3**, 1200–1225 (2019).
11. Li, J. et al. Electrocaloric effect in $BaTiO_3$ multilayer capacitors with first-order phase transitions. *J. Phys. Energy* **5**, 024017 (2023).
12. Lines, M. E. & Glass, A. M. *Principles and Applications of Ferroelectrics and Related Materials* (Clarendon Press, 1977).
13. Neese, B. et al. Large electrocaloric effect in ferroelectric polymers near room temperature. *Science* **321**, 821–823 (2008).
14. Qi, H., Chen, L., Deng, S. & Chen, J. High-entropy ferroelectric materials. *Nat. Rev. Mater.* **8**, 355–356 (2023).
15. Zhang, Q. M. & Zhang, T. The refrigerant is also the pump. *Science* **357**, 1094–1095 (2017).
16. Scott, J. F. Applications of modern ferroelectrics. *Science* **315**, 954–959 (2007).
17. Mischenko, A. S., Zhang, Q., Scott, J. F., Whatmore, R. W. & Mathur, N. D. Giant electrocaloric effect in thin film $PbZr_{0.95}Ti_{0.05}O_3$. *Science* **311**, 1270–1271 (2006).
18. Li, Y. L., Cross, L. E. & Chen, L. Q. A phenomenological thermodynamic potential for $BaTiO_3$ single crystals. *J. Appl. Phys.* **98**, 64101 (2005).
19. Liang, L., Li, Y. L., Chen, L. Q., Hu, S. Y. & Lu, G. H. Thermodynamics and ferroelectric properties of $KNbO_3$. *J. Appl. Phys.* **106**, 104118 (2009).
20. Dougherty, T. P. et al. Femtosecond resolution of soft mode dynamics in structural phase transitions. *Science* **258**, 770–774 (1992).
21. Li, F., Zhang, S., Damjanovic, D., Chen, L. Q. & Shrout, T. R. Local structural heterogeneity and electromechanical responses of ferroelectrics: learning from relaxor ferroelectrics. *Adv. Funct. Mater.* **28**, 1801504 (2018).
22. Pan, H. et al. Ultrahigh-energy density lead-free dielectric films via polymorphic nanodomain design. *Science* **365**, 578–582 (2019).
23. Pan, H. et al. Ultrahigh energy storage in superparaelectric relaxor ferroelectrics. *Science* **374**, 100–104 (2021).
24. Li, J. et al. Complex phase transitions and associated electrocaloric effects in different oriented PMN-30PT single crystals under multi-fields of electric field and temperature. *Acta Mater.* **182**, 250–256 (2020).
25. Chukka, R. et al. Orientation dependence of electrocaloric effects in $Pb(Zn_{1/3}Nb_{2/3})$-$PbTiO_3$ single crystals. *AIP Adv.* **3**, 072118 (2013).
26. Li, H. et al. First-principles study on the structural, elastic, piezoelectric and electronic properties of ($BaTiO_3$, $LiTaO_3$)-modified $KNbO_3$. *Mater. Today Commun.* **26**, 102092 (2021).
27. Magome, E. et al. Crystal structure of $BaTiO_3$-$KNbO_3$ nanocomposite ceramics: relationship between dielectric property and structure of heteroepitaxial interface. *Jpn. J. Appl. Phys.* **51**, 09LE05 (2012).
28. Huang, Y., Zhao, C., Wu, B. & Wu, J. Multifunctional $BaTiO_3$-based relaxor ferroelectrics toward excellent energy storage performance and electrostrictive strain benefiting from crossover region. *ACS Appl. Mater. Interfaces* **12**, 23885–23895 (2020).
29. Zhang, M. et al. Ultrahigh energy storage in high-entropy ceramic capacitors with polymorphic relaxor phase. *Science* **384**, 185–189 (2024).
30. Sarkar, A. et al. Influence of neutron and gamma irradiation on the electrocaloric properties of Mn-doped $0.9Pb(Mg_{1/3}Nb_{2/3})O_3$-$0.1PbTiO_3$ ceramics. *J. Phys. Energy* **5**, 045006 (2023).
31. Khansur, N. H., Kawashima, H., Wada, S., Hudspeth, J. M. & Daniels, J. Enhanced extrinsic domain switching strain in core-shell structured $BaTiO_3$-$KNbO_3$ ceramics. *Acta Mater.* **98**, 182–189 (2015).
32. Seabaugh, M. M., Suvaci, E., Brahmaroutu, B. & Messing, G. L. Modeling anisotropic single crystal growth kinetics in liquid phase sintered α-Al_2O_3. *Interface Sci.* **8**, 257–267 (2000).
33. Li, J. et al. Lead zirconate titanate ceramics with aligned crystallite grains. *Science* **380**, 87–93 (2023).
34. Liu, J. et al. Piezoelectric ceramic hardening through defect distribution optimization in multicomponent systems. *Adv. Funct. Mater.* **35**, 2413130 (2024).
35. Li, Y. et al. Enhanced energy storage performance in NBT-based MLCCs via cooperative optimization of polarization and grain alignment. *Nat. Commun.* **15**, 8958 (2024).
36. Fu, J., Hou, Y., Zheng, M. & Zhu, M. Topochemical conversion of (111) $BaTiO_3$ piezoelectric microplatelets using $Ba_6Ti_{17}O_{40}$ as the precursor. *Cryst. Growth Des.* **19**, 1198–1205 (2019).
37. Yang, S. et al. Textured ferroelectric ceramics with high electromechanical coupling factors over a broad temperature range. *Nat. Commun.* **12**, 1414 (2021).
38. Kou, Q. et al. Tetragonal (Ba, Ca)(Zr, Ti)O_3 textured ceramics with enhanced piezoelectric response and superior temperature stability. *J. Mater.* **8**, 366–374 (2022).
39. Messing, G. L. et al. Templated grain growth of textured piezoelectric ceramics. *Crit. Rev. Solid State Mater. Sci.* **29**, 45–96 (2004).
40. Li, F., Jin, L., Xu, Z. & Zhang, S. Electrostrictive effect in ferroelectrics: an alternative approach to improve piezoelectricity. *Appl. Phys. Rev.* **1**, 011103 (2014).
41. Li, J. et al. Grain-orientation-engineered multilayer ceramic capacitors for energy storage applications. *Nat. Mater.* **19**, 999–1005 (2020).
42. Park, S. E. & Shrout, T. R. Ultrahigh strain and piezoelectric behavior in relaxor based ferroelectric single crystals. *J. Appl. Phys.* **82**, 1804–1811 (1997).
43. Bell, A. J. Phenomenologically derived electric field-temperature phase diagrams and piezoelectric coefficients for single crystal barium titanate under fields along different axes. *J. Appl. Phys.* **89**, 3907–3914 (2001).
44. Wada, S., Kakemoto, H. & Tsurumi, T. Enhanced piezoelectric properties of piezoelectric single crystals by domain engineering. *Mater. Trans.* **45**, 178–187 (2004).
45. Cao, X. et al. Enhanced electrocaloric effect in $(Bi_{0.5}Na_{0.5})TiO_3$-$6BaTiO_3$ based relaxor ferroelectric nanocomposites by regulating Joule heating. *Chem. Eng. J.* **495**, 153061 (2024).
46. Uršič, H. et al. High radiation tolerance of electrocaloric (1-*x*)$Pb(Mg_{1/3}Nb_{2/3})O_3$-x$PbTiO_3$. *J. Eur. Ceram. Soc.* **42**, 5575–5583 (2022).
47. Lotgering, F. K. Topotactical reactions with ferrimagnetic oxides having hexagonal crystal structures-I. *J. Inorg. Nucl. Chem.* **9**, 113–123 (1959).
48. Guo, J. et al. Evolution of ferroelectricity in $Sr_{0.6}Ba_{0.4}Nb_2O_6$-$BaTiO_3$ solid solution with a strong electrocaloric effect. *ACS Appl. Mater. Interfaces* **16**, 43704–43712 (2024).
49. Zhang, C. et al. Substantially enhanced electrocaloric effect in $Ba(Zr_{0.2}Ti_{0.8})O_3$ lead-free ferroelectric ceramics via lattice stress engineering. *ACS Appl. Mater. Interfaces* **15**, 18065–18073 (2023).
50. Qian, X. S. et al. Giant electrocaloric response over a broad temperature range in modified $BaTiO_3$ ceramics. *Adv. Funct. Mater.* **24**, 1300–1305 (2014).
51. Lin, W. et al. Achieving ultrahigh electrocaloric response in $(Bi_{0.5}Na_{0.5})TiO_3$-based ceramics through B-site defect engineering. *ACS Nano* **18**, 13322–13332 (2024).
52. Jian, X. D. et al. Enhanced electrocaloric effect in Sr^{2+}-modified lead-free $BaZr_xTi_{1-x}O_3$ ceramics. *ACS Appl. Mater. Interfaces* **11**, 20167–20173 (2019).
53. Wen, L. et al. Comprehending the underlying mechanism behind directly/indirectly obtained large electrocaloric response in

$Bi_{0.5}Na_{0.5}TiO_3$-based relaxor ferroelectrics. *Acta Mater*. **255**, 119090 (2023).
54. Tao, H. et al. Large electrocaloric effect under electric field behavior in potassium sodium niobate ceramics with incompletely overlapped phase boundaries. *J. Mater. Chem. A* **10**, 5262–5272 (2022).

Acknowledgments

J.L. and F.L. acknowledge the support of the National Natural Science Foundation of China-NSAF under Grants 52325205, 52422207, 52172129, and Qin Chuangyuan high-level innovation and entrepreneurship talent project QCYRCXM-2022-318, Qin Chuangyuan "scientist + engineer" team construction 2023KXJ-025, Shaanxi Provincial Key R&D Program Qinchuangyuan General Platform 'Four-Chain Integration' 2024PT-ZCK-14 and Baoding science and technology plan project 2394G013. The authors would like to express their gratitude to Mr. Zijun Ren and Mr. Haitao Fan at Instrument Analysis Center of Xi'an Jiaotong University for their assistance with SEM-EBSD analysis.

Author contributions

The work was conceived and designed by X.L., J.L., and F.L.; X.L. fabricated the samples and performed the microstructure experiments; X.L., Y.L., and J.L. assisted the fabrication of templates and textured ceramics; X. Liu, S.Y., J.W., D.H., and J.Z. assisted the properties measurements for the samples; H.W., Y.Z., X.D., J.S., H.D., and S.Z. supervised the fabrication and test of the samples; X.L., H.D., and J.L. drafted the manuscript; F.L. revised the manuscript; and all authors discussed the results.

Competing interests

The authors declare no competing interests.

Additional information

Supplementary information The online version contains supplementary material available at https://doi.org/10.1038/s41467-025-59808-w.

Correspondence and requests for materials should be addressed to Jinglei Li, Hongliang Du or Fei Li.

Peer review information *Nature Communications* thanks Soukaina Merselmiz, and the other, anonymous, reviewer(s) for their contribution to the peer review of this work. A peer review file is available.